Manipulating the Optically Active Defect–Defect Interaction of Colloidal Quantum Dots for Carbon Dioxide Photoreduction

Mengke Cai, Xin Tong, Peisen Liao, Shujie Shen, Hongyang Zhao, Xin Li, Li Xia, Huaqian Zhi, Nan Zhou, Ziqian Xue, et al.

Manipulating the Optically Active Defect-Defect Interaction of Colloidal Quantum Dots for Efficient Carbon Dioxide Photoreduction

Mengke Cai[a,b], Xin Tong[a,b]*, Peisen Liao[c], Shujie Shen[a], Hongyang Zhao[a], Xin Li[a], Li Xia[a], Huaqian Zhi[a], Nan Zhou[a], Ziqian Xue[d], Lei Jin[a,e], Jieyuan Li[a], Guangqin Li[c], Fan Dong[a], Andrei V. Kabashin[f], and Zhiming M. Wang[a,b,g]*

[a] *Institute of Fundamental and Frontier Sciences, University of Electronic Science and Technology of China, Chengdu 610054, China*

[b] *Yangtze Delta Region Institute (Huzhou), University of Electronic Science and Technology of China, Huzhou 313001, China*

[c] *MOE Laboratory of Bioinorganic and Synthetic Chemistry, Lehn Institute of Functional Materials, School of Chemistry, Sun Yat-Sen University, Guangzhou 510275, China*

[d] *Institute for Integrated Cell-Material Sciences, Kyoto University, Kyoto 606-8501, Japan*

[e] *Centre for Energy, Materials and Telecommunications, Institut national de la Recherche Scientifique, Varennes J3X 1P7, Canada*

[f] *Aix-Marseille University, Centre national de la recherche scientifique, Marseille 13009, France*

[g] *Institute for Advanced Study, Chengdu University, Chengdu 610106, China*

*E-mail: xin.tong@uestc.edu.cn; zhmwang@uestc.edu.cn

KEYWORDS: *quantum dots; defects engineering; photocatalysis; carbon dioxide reduction; solar-to-fuel conversion.*

ABSTRACT: Defect engineering in colloidal quantum dots (QDs), a typical photocatalytic material, is promising to tailor the optoelectronic properties and achieve efficient solar-to-fuel energy conversion. However, understanding the effect of defect-defect interaction on both charge carrier and catalytic dynamics is still challenging. Here, we report a class of defect-engineered copper-deficient Zn-doped $CuInS_2$ (ZCIS) QDs that synergistically utilize copper vacancy and Cu^{2+} defect states to realize efficient CO_2 photoreduction. Steady and transient optical characterizations reveal that the density of copper vacancy can manipulate the distribution of optically active Cu^+ and Cu^{2+} defect states (appearing as Cu_{In}'' and $Cu_{Cu}^{\bullet}$ species, respectively), wherein the Cu^+ defect states suppress interband absorption and sharpen the Shockley-Read-Hall (SRH) recombination, while Cu^{2+} defect states enables the prolonged exciton lifetime of QDs. *In situ* infrared spectroscopic investigations and theoretical density functional calculation (DFT) demonstrate the photoactive Cu^{2+} defect states nearby copper vacancy in ZCIS QDs can effectively activate CO_2 to the COOH* intermediates, leading to a remarkable photocatalytic CO production rate up to 532.3 μmol g^{-1} h^{-1} (turnover number ~ 1963) after 120 h illumination.

1. INTRODUCTION

To build a sustainable future for human communities, the utilization of CO_2 as carbon source and solar energy as driving force to generate fuel is of great significance.[1-3] Efficient solar fuel generation relies on high-performance photocatalysts, which can effectively absorb sunlight and utilize charge carriers for desirable chemical reaction.[4-5] However, the entire photocatalytic conversion processes include complex photo-physical and catalytic-chemical steps, bringing great challenge to design efficient photocatalysts.[6-7]

The atoms form a regular lattice in crystalline materials, which is disrupted by defects. In this manner, various defect states appear and strongly affect the band structure. For instance, oxygen vacancies in black TiO_2 is able to broaden the light absorption range from ultraviolet to infrared.[8] Therefore, controlling defects in photocatalysts is essential yet complex.[9-10] On the one hand, defects can limit the transport of charge carriers, serving as Shockley-Read-Hall (SRH) recombination centers.[11] On the other hand, they are important for introducing sub-band states, tuning Fermi level and selectively capturing desirable charge carriers.[12] Besides, both steric configuration and electronic structure of photocatalysts are related to defects,[13-14] which can affect the processes of photocatalysis including photo-physical carrier dynamics and catalytic-chemical interface dynamics.[15-16] Theoretically, there are many types of point defects in photocatalysts, including interstitial, antisite and vacancy with

variable defect state charge, which are usually accompanied due to charge compensation and atomic conservation.[17] Specifically, vacancies in the nonstoichiometric compounds have been commonly reported for solar energy conversion applications.[18-19] However, the current research mainly focuses on vacancies themselves, ignoring other associated defects and defect-defect interactions.[13-16, 18-20] Therefore, it is very important to delicately probe the effect of defect-defect interactions on the charge carriers and photocatalytic processes.

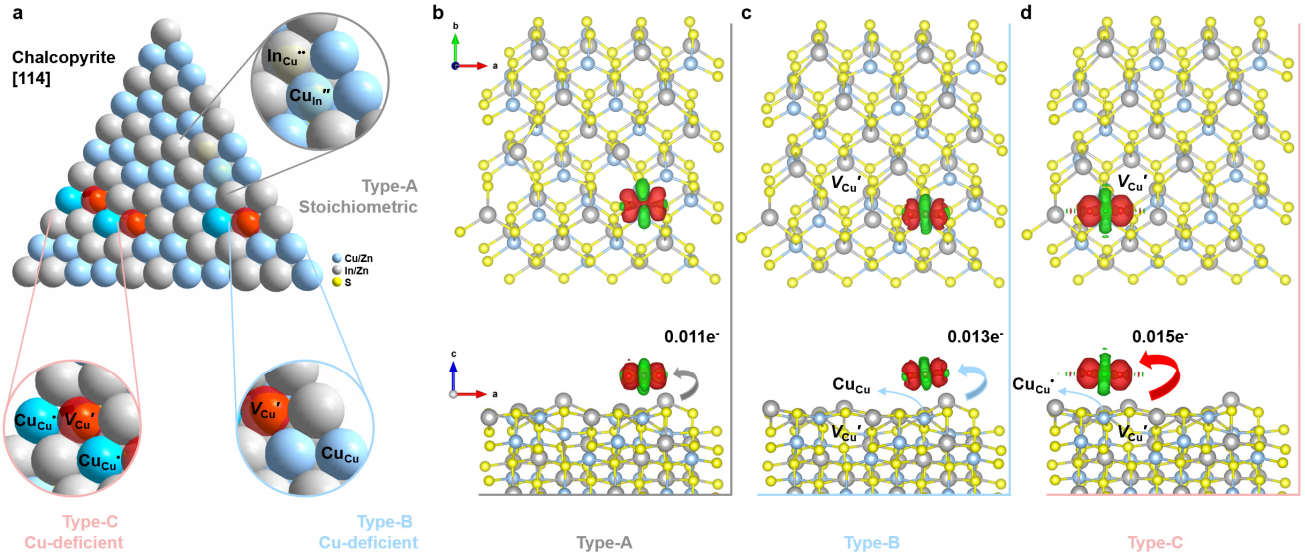

Figure 1. Manipulation of QDs' defect states and their effect on the CO_2 adsorption. (a) Schematic illustration for different defect state types in stoichiometric and Cu-deficient QDs. Hypothetical CO_2 adsorption configuration on (b) Type-A stoichiometric, (c) Type-B and (d) Type-C Cu-deficient QDs.

Colloidal quantum dots (QDs) are promising photocatalysts due to cost-effectiveness and tunable optoelectrical properties.[21-22] Herein, we choose highly defect-tolerant I-III-VI_2 $CuInS_2$ colloidal QDs as model photocatalysts, where the highly off-stoichiometric composition allows for the clear distinction of varied defects.[23-26] To enhance the stability and increase the band gap of narrow gap ternary $CuInS_2$ QDs, the Zn-doped $CuInS_2$ (ZCIS) QDs with varied Cu-to-(Zn+In) ratios are prepared, as noted from 8/12ZCIS to 1/12ZCIS (Details in Supporting Information). In particular, the ratio of Cu-to-In is near stoichiometric in 8/12ZCIS QD sample. As shown in Figure 1a, the prevailing defects are antisite Cu_{In}''-$In_{Cu}^{\bullet\bullet}$ pairs in Type-A stoichiometric QDs, as expressed by the following defect reaction equation according to the Kröger-Vink notations:[25, 27]

$$Cu_{Cu} + In_{In} \rightarrow Cu_{In}'' + In_{Cu}^{\bullet\bullet} \quad (1)$$

The copper defect (Cu_{In}'') is in the oxidation state of 1+,[27] while decreasing the copper content can contribute to the generation of Type-B Cu-deficient ZCIS QDs, promoting the formation of copper vacancies (V_{Cu}').[24] Following the accumulation of copper vacancies, the Cu_{Cu} nearby copper vacancy transforms into Cu^{2+} defect states ($Cu_{Cu}^{\bullet}$) due to charge compensating in Type-C Cu-deficient ZCIS QDs,[25] illustrated by the following equation.

$$Null + Cu_{Cu} \rightarrow V_{Cu}' + Cu_{Cu}^{\bullet} \quad (2)$$

which were demonstrated by the electron paramagnetic resonance (EPR) and femtosecond transient absorption (fs-TA) measurements. The fs-TA photodynamic analysis of ZCIS QDs reveals: i) Cu^{2+} defect states promote interband absorption, while Cu^{+} defect states participate in the intraband transition. ii) adjacent $Cu_{Cu}^{\bullet}$-V_{Cu}' defect pairs suppress the deep trap-assisted SRH recombination and promote electron trapping to shallow trap states. iii) Cu-deficient QDs with Cu^{2+} defect states show stronger and longer-lived excited states absorption. *In situ* diffuse reflectance infrared Fourier transform spectra (DRIFTS) measurements and density functional theory (DFT) calculations disclosed that the adjacent $Cu_{Cu}^{\bullet}$-V_{Cu}' defect pairs can serve as effective surface sites for CO_2 adsorption and activation, leading to the accumulated CO_2^{-} species on Cu-deficient QDs with Cu^{2+} defect states. Besides, the configuration of $Cu_{Cu}^{\bullet}$-V_{Cu}' defect pairs can effectively reduce the reaction energy barrier of the rate-limiting step from CO_2* species to COOH* intermediates. Benefiting from the synergetic defect-defect interaction, the well-designed Type-C Cu-deficient ZCIS QDs achieved durable and efficient CO_2 photoreduction to CO in aqueous solutions, with a selectivity of 92% and a remarkable yield rate of 532.3 μmol g^{-1} h^{-1} after 120 h illumination (turnover number ~1963 based on the QDs). To further verify the practicability, the natural sunlight-driven CO_2 photoreduction experiments are conducted in outdoor environment for one month, endowing the great promise in future carbon neutrality.

2. RESULTS AND DISCUSSION

Theoretical simulations were first performed to predict the affinity between copper defect sites and CO_2 molecules,[28] wherein the relevant electron transfer capacities of three ideal Cu defect states (Type-A, B, C, Figure 1b-d) in ZCIS QDs (Figure S1)

were investigated. The opimized sturcture parameters are given in Table S1. It reveals that Cu^{2+} defect sites nearby copper vacancy are more compatible with CO_2 (0.015 e^- per CO_2 molecule), which exhibited more variation in bond length (1.175~1.176 Å) and bond angle (179.32°) toward the CO_2 than other Cu sites. In light of this finding, it is desirable to synthesize Type-C Cu-deficient QDs containing $Cu_{Cu}^{\bullet}$-V_{Cu}' defect pairs for CO_2 photoreduction. Accordingly, we prepared the Type-A stoichiometric colloidal QDs (denoted as 8/12ZCIS) with a Cu/In feed ratio of 1:1, whereafter the Cu-deficient QDs with controlled composition including 4/12ZCIS, 2/12ZCIS and 1/12ZCIS were synthesized by reducing the content of Cu precursor (CuI) during QDs' synthesis. To gain the actual ratios of Cu/In in the QDs, inductively coupled plasma-optical emission spectroscopy (ICP-OES) was performed, showing atomic Cu/In ratios of 0.97, 0.43, 0.26 and 0.13 in the 8/12ZCIS, 4/12ZCIS, 2/12ZCIS and 1/12ZCIS QDs (Table S2), respectively, which are almost consistent with the Cu-to-In feed ratios.

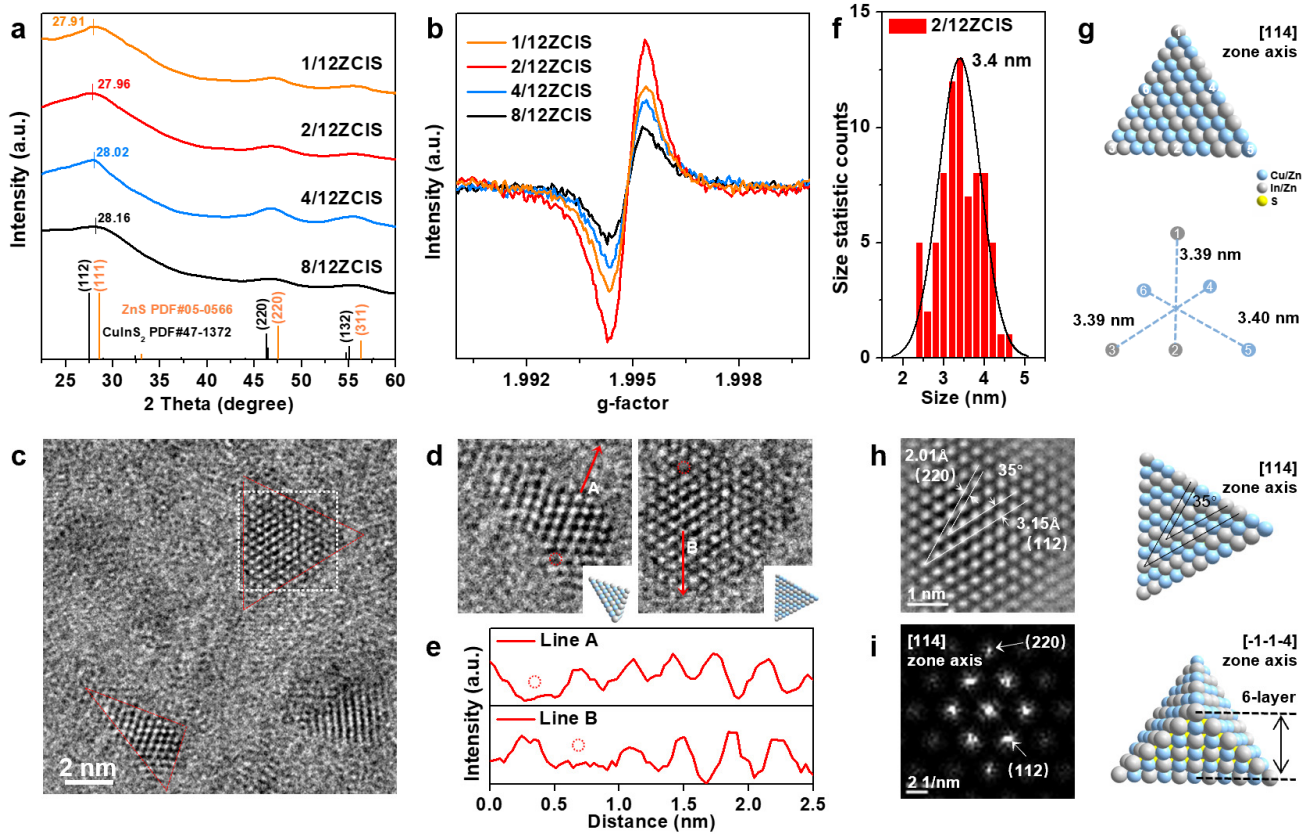

Figure 2. Structure characterization of QDs. (a) XRD patterns and (b) EPR spectra of as-prepared ZCIS QDs. (c) TEM image, (d) partial magnification of red triangle area in c, (e) intensity profile corresponding to the red arrow in d, (f) size statistics, (g) structure model, (h) crystal plane parameters and (i) Fourier transform analysis of the white dotted area in c for Cu-deficient 2/12ZCIS QDs.

X-ray diffraction (XRD) patterns of as-prepared ZCIS QDs in Figure 2a show a typical chalcopyrite phase of the QDs, wherein the 8/12ZCIS QDs exhibited a main diffraction peak between the (112) plane of chalcopyrite $CuInS_2$ and the (111) plane of sphalerite ZnS, which is attributed to the incorporation of zinc dopants into chalcopyrite $CuInS_2$ QDs.[29-30] Notably, the diffraction peak slightly shifts towards lower angles from stoichiometric 8/12ZCIS to Cu-deficient 1/12ZCIS QDs (Figure 2a), which may be due to that Cu-deficient vacancy defects can create voids in QDs and result in increased lattice spacing.[31] The concentration of defects in the QDs was probed using electron paramagnetic resonance (EPR) spectra, which exhibited strong signals around g=1.995, indicating the presence of copper vacancies (Figure 2b).[14] Meanwhile, the tested highest EPR signal intensity of the 2/12ZCIS sample indicate the most abundant vacancy defects among these QDs. Transmission electron microscopy (TEM) characterization of the QDs showed a typical pyramidal shape with a high degree of uniformity based on different orientations (Figure 2c and 2d), with line intensity profiles demonstrating the presence of abundant vacancies in Cu-deficient 2/12ZCIS QDs (Figure 2e).[32] As displayed in Figure 2f and S2, the measured average diameter of 3.2~3.4 nm is in accordance with the crystallographic model of trigonal pyramidal six-layer metal atoms in size (Figure 2g, the model details can be found in Figure S3). The d_{112} and d_{220} spacings are measured to be 0.315 and 0.201 nm (Figure 2h), and the corresponding dihedral angle of 35° matches well with the calculated angle between (112) and (220) planes by using the following equation:

$$\cos\phi = \frac{\frac{h_1h_2+k_1k_2}{a^2}+\frac{l_1l_2}{c^2}}{\sqrt{\left(\frac{h_1^2+k_1^2}{a^2}+\frac{l_1^2}{c^2}\right)\left(\frac{h_2^2+k_2^2}{a^2}+\frac{l_2^2}{c^2}\right)}} \quad (3)$$

where ϕ, a, b and c are the dihedral angle and unit cell parameters, respectively, testifying the [114] orientation of as-synthesized QDs, as further verified by the associated Fourier transform analysis in Figure 2i. The results demonstrate the successful synthesis of the pyramidal ZCIS QDs along the [114] orientation with six-layer metal atoms and tunable Cu vacancy concentrations.

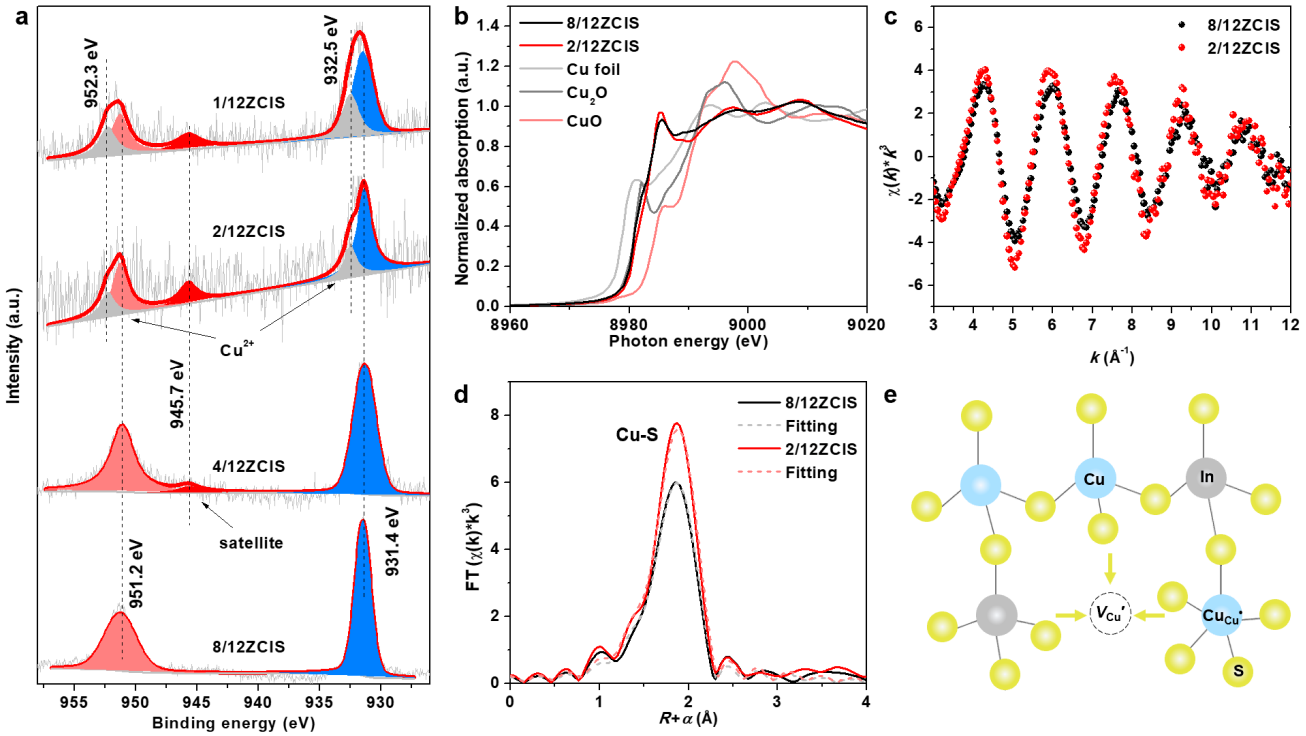

Figure 3. Identification of Cu defect states in QDs. (a) High-resolution XPS Cu 2p spectra of as-prepared QDs. (b) Cu K-edge XANES data of 8/12ZCIS, 2/12ZCIS QDs and reference samples. (c) Cu K-edge EXAFS of oscillations shown in k^3-weighted *k*-space. (d) Cu K-edge EXAFS (lines) and the curve-fitting (dotted line) for 8/12ZCIS and 2/12ZCIS QDs shown in k^3-weighted *R*-space. The data are not phase-corrected. (e) Cu vacancy in tetrahedral coordinated chalcopyrite results in a structural relaxation, thus local disorder increases the coordination number of nearby Cu atoms.

X-ray photoelectron spectroscopy (XPS) was carried out to study the Cu defect states in various QD samples (Figure 3a and Figure S4-5). As compared to the 8/12ZCIS and 4/12ZCIS QDs, the peak of Cu $2p_{3/2}$ of 2/12ZCIS QDs shifts to higher binding energies, which is indicative of the increased Cu valence state.[33-34] The deconvoluted peaks centered at 931.4 eV (Cu $2p_{3/2}$) and 951.2 eV (Cu $2p_{1/2}$) are assigned to Cu^{1+}, whereas the additional peaks at 932.5 eV and 952.3 eV are ascribed to Cu^{2+} appeared in 2/12ZCIS QDs.[14-16, 35] More importantly, the Cu $2p_{3/2}$ satellite peak at 945.7 eV (defined as the presence of Cu^{2+} species) can reach the maximum proportion of 20% in 2/12ZCIS QD sample,[36] thus proving the existence of more Cu^{2+} defect states in the Cu-deficient 2/12ZCIS QDs. Cu K-edge X-ray absorption spectroscopy (XAS) was conducted to further identify the local environment of Cu defect states. As shown in Figure 3b, the X-ray absorption near-edge structure (XANES) spectra exhibit the sharp lines corresponding to the electron transition from Cu 1*s* to 3*d* orbitals.[37] The absorption peaks appeared at ~8981 eV of 8/12ZCIS and 2/12ZCIS QDs indicate both QDs have the same Cu^+ species as Cu_2O reference sample. A slight forward offset of peak for 2/12ZCIS QDs proves the increased Cu valence state.[38] The similar Cu K-edge EXAFS of oscillations shown in k^3-weighted *k*-space suggest that both QDs have analogous local coordination geometry of Cu^+ ions (Figure 3c). Notably, 2/12ZCIS QDs show more amplitude oscillations, suggesting the average coordination number of Cu atom increases after introducing Cu vacancies. To examine the local coordination environment changes, we performed the extended X-ray absorption fine structure (EXAFS) measurements and t specific fitting details are attached in Table S3 and Figure S6. The curve fitting reveals that the coordination number of Cu-S for 2/12ZCIS QDs is 4.8±0.3 (Figure 3d), which is larger than that of 8/12ZCIS QDs (3.8±0.2). As shown in Figure 3e, the formation of Cu vacancy could create a void with dangling bonds on the nearby Cu atoms,[39] hence we speculate that there would be more space and freedom for Cu atoms to interact with S anions. These findings manifest that introducing Cu vacancies perhaps induced local structural relaxation of surrounded Cu^+ sites, thus overcoming the limitation of tetrahedral coordination.

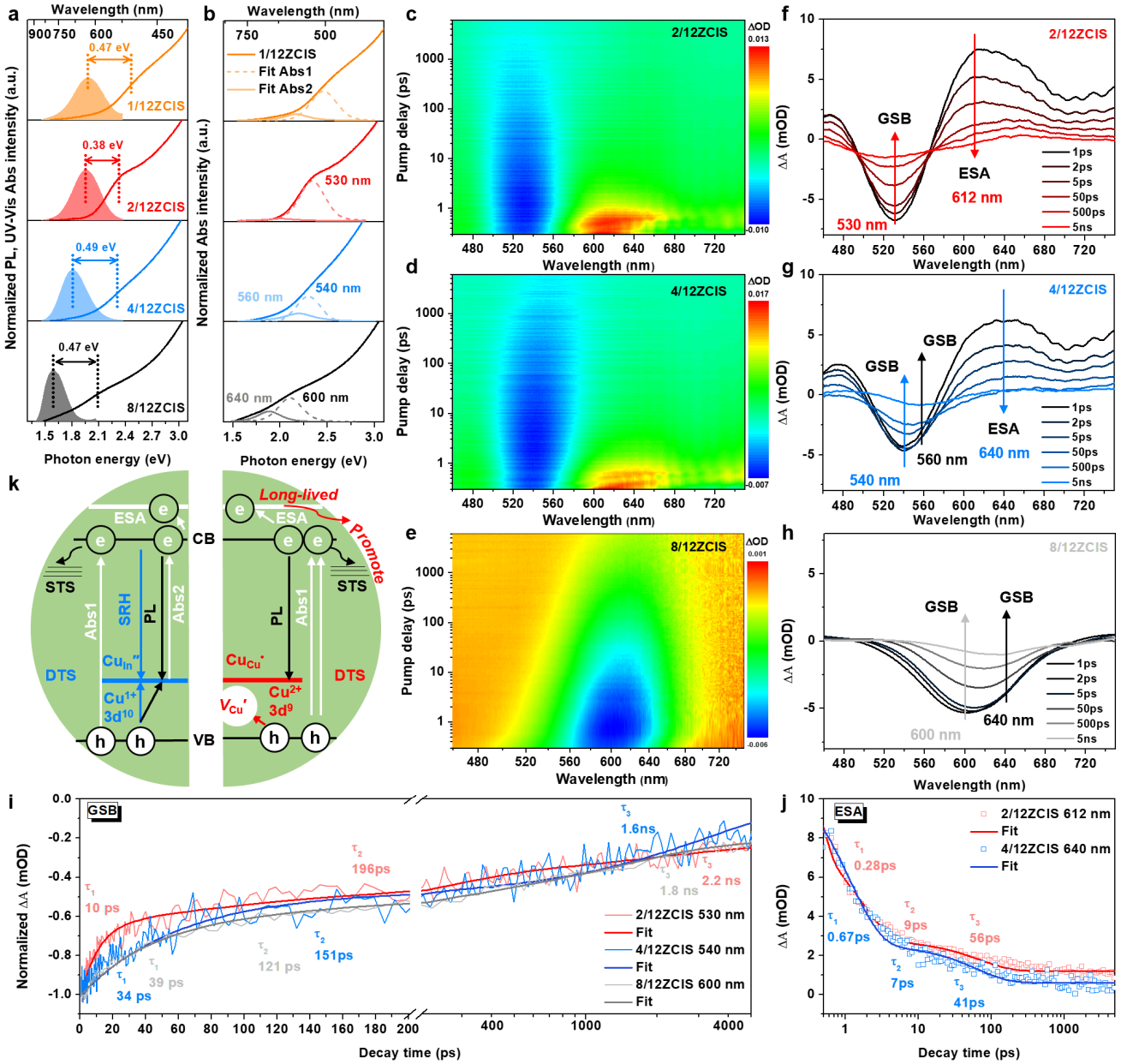

Figure 4. Optical spectral analysis of photo-induced charge carriers. (a) UV-vis absorption (lines) and PL emission (colored shading) spectra of ZCIS QDs. (b) Recognition of UV-vis absorption peaks. Insets: the absorption edge consists of features from both the interband VB-CB transition (dotted line) and the intraband Cu-CB transition (dashed line). (c, d, e) 3D contour plots of fs-TA spectra. The fs-TA spectra of (c, f) 2/12ZCIS, (d, g) 4/12ZCIS and (e, h) 8/12ZCIS QDs. The kinetic traces of GSB (i) and ESA (j) signals. (k) Schematic depiction of charge carriers' dynamics involved in ZCIS QDs with Cu^{1+} (left) and Cu^{2+} (right) defect states. In both cases, emission originates from the transition involving a CB electron and a hole-like intragap Cu defect states (black straight arrow), thus accounting for the large Stokes shift. In the case of the Cu^{1+} defect, intragap Cu^{1+}-CB transition (Abs2) leads to an additional near band-edge feature compared with VB-CB transition (Abs1), while Cu^{2+} defect is optically absorption-passive.

To further confirm the existence of Cu defect states and understand relevant charge kinetics in the QDs, ultraviolet-visible (UV-vis) absorption, photoluminescence (PL) emission and fs-TA tests were conducted and shown in Figure 4. The band gap (E_g) of QDs is calculated to be ~2.14-2.46 eV based on the minimum of the second derivative of the absorption spectra (Figure S7), which represents the band-edge transition between conduction band (CB) and valance band (VB) in quantum-confined semiconductor materials such as QDs.[40] A large Stokes shift (380~490 meV) between PL emission and exciton absorption peak of QDs is observed in Figure 4a, in which the Cu-related defects in the QDs are responsible for such large Stokes shift due to intragap emission,[24, 27, 41] as a result of both the emissive Cu^{1+} and Cu^{2+} defect states.[25, 27] However, these two defect states cause distinct features on the absorption spectra. In particular, the Cu^{1+} defect states remain absorption-active as one

of the 3d electrons can be excited into CB states from the $3d^{10}$ to $3d^{9}$ configuration.[27] In contrast, no significant intragap absorption feature is observed in the latter since the Cu^{2+} defect states (induced by V_{Cu}') have the $3d^{9}$ configuration that can't be transformed into $3d^{8}$ state, causing the band-edge absorption.[27] Therefore, in comparison to the band-edge absorption (exciton transition peak fitted as Abs1),[24] the Cu^{1+}-CB transition is expected to exhibit an intragap absorption feature (a tail absorption peak fitted as Abs2) in the near-band-edge region (Figure 4b). As summarized in Table S4, the band-edge absorption is more apparent in the optical characterizations of Cu-deficient 2/12ZCIS QDs, revealing the presence of dominant Cu^{2+} defect states in this sample.

Ultrafast fs-TA measurements were performed to further figure out the details of these Cu defect states (excited at 387 nm with power intensity of 14 μJ cm^{-2}, under continuous stirring), as shown in Figure 4c-h. Note that the ground state bleaching (GSB) signal recorded with Cu-deficient 2/12ZCIS QDs (Figure 4c and 4f) shows different spectral features such as a more symmetrical and narrower bleaching signal compared to that of the 4/12ZCIS QDs, 8/12ZCIS or reported stoichiometric samples.[24, 42-43] In the case of the 4/12ZCIS QDs (Figure 4d and 4g), the asymmetrical and broad bleaching can split into two components including band-edge (540 nm) and intragap (560 nm) transitions,[24] which is consistent with the results of steady-state absorption spectrum. Moreover, the splitting of GSB peak for stoichiometric 8/12ZCIS QDs is obvious and clear (Figure 4e and 4h), where different band-edge (600 nm) and intragap (640 nm) transitions can be observed. Conversely, we observed a single band-edge transition (530 nm) in the 2/12ZCIS QDs (Figure 4f), confirming that the Cu-deficient 2/12ZCIS QDs mainly contains Cu^{2+} defect states accompanied with copper vacancy as $Cu_{Cu}^{\bullet}$-V_{Cu}' defect pairs. Furthermore, the charge carriers' dynamics were investigated *via* kinetics fitting of GSB and excited-state absorption (ESA) signals to reveal the effect and interaction of Cu defect states in the QDs, and the fitting parameters are listed in Table S5. The GSB signal is attributed to the state filling of CB electron with negligible contribution from VB hole due to higher degeneracy of the hole levels, thereby indicating the CB electron population decay.[44] The tri-exponential fitting recover features are spread out in Figure 4i: (i) The short decay kinetics of 2/12ZCIS QDs with a time of ~10 ps (τ_1) is faster than that of the 4/12ZCIS QDs (τ_1=34 ps) and 8/12ZCIS QDs (τ_1=39 ps), reflecting favorable electron trapping in shallow trap states (STS) near CB.[9, 40, 45-46] (ii) The following hundreds of picoseconds (e.g., 121-196 ps) are traced to the exciton cooling.[45] (iii) The longer delay up to nanoseconds (1.6-2.2 ns in ZCIS QDs) refers to the nonradiative recombination of SRH recombination pathway.[9] Despite both the Cu^{2+} and Cu^{+} defect states are deep trap states (DTS), the SRH recombination is distinct due to that the Cu^{2+} defect as a hole-like state ($3d^{9}$) can recombine quickly with CB electron, while Cu^{+} defect must capture a VB hole and restore its 2+ oxidation state (from $3d^{10}$ to $3d^{9}$) before completing the recombination processes.[27] Therefore, the SRH recombination is competitive to Cu^{+} defect-mediated radiative recombination due to similar hole capture mechanism, while the abundant Cu vacancies can effectively remove the VB hole to suppress the nonradiative recombination in 2/12ZCIS QDs.[25, 27] Eventually, the SRH recombination decay time of 2/12ZCIS QDs (τ_3=2.2 ns) is slower than that of the 4/12ZCIS QDs (GSB, τ_3=1.6 ns) and 8/12ZCIS QDs (GSB, τ_3=1.8 ns), indicating that the $Cu_{Cu}^{\bullet}$-V_{Cu}' defect pairs are able to suppress nonradiative recombination and promote slow exciton relaxation.[45, 47]

In addition, as shown in Figure 4j and Table S5, the slower decay of ESA signal of 2/12ZCIS QDs (τ_{av} = 41 ps) indicates the higher possibility of active electron utilization and transfer to electron acceptors with respect to the ESA signal of 4/12ZCIS QDs (τ_{av} = 29 ps).[45, 48] This conclusion is further supported by measuring the fs-TA dynamics, wherein the benzoquinone (BQ) molecules were used to remove the active electrons in QDs' aqueous solution [44, 49]. As shown in Figure S8, the TA spectra of 2/12ZCIS-BQ complexes showed a faster recovery of the GSB signal with an average lifetime (1088 ps) compared to that (1977 ps) of the 2/12ZICS QDs. Due to the limited time scale of the fs-TA experiment (up to 6 ns), further information about the electron transfer processes on the nanosecond scale was obtained from time-resolved PL (tr-PL) of QDs. The electron-transfer time (τ_{et}) is estimated by the following equation:[50]

$$1/\tau_{et} = 1/\tau_{av,100mM\ BQ} - 1/\tau_{av,0mM\ BQ} \qquad (4)$$

A fairly fast electron transfer with τ_{et} of 34 ns for 2/12ZCIS QDs is observed (Figure S9 and Table S6) among four types of QD samples, which exactly benefits from the long-lived active excitons. To summarize, Figure 4i visually depicts the overall charge dynamics involved in ZCIS QDs. Due to the presence of $Cu_{Cu}^{\bullet}$-V_{Cu}' defect pairs, the Type-C Cu-deficient 2/12ZCIS QDs with long-lived active charge carriers and inhibited nonradiative recombination are more promising for CO_2 photoreduction.

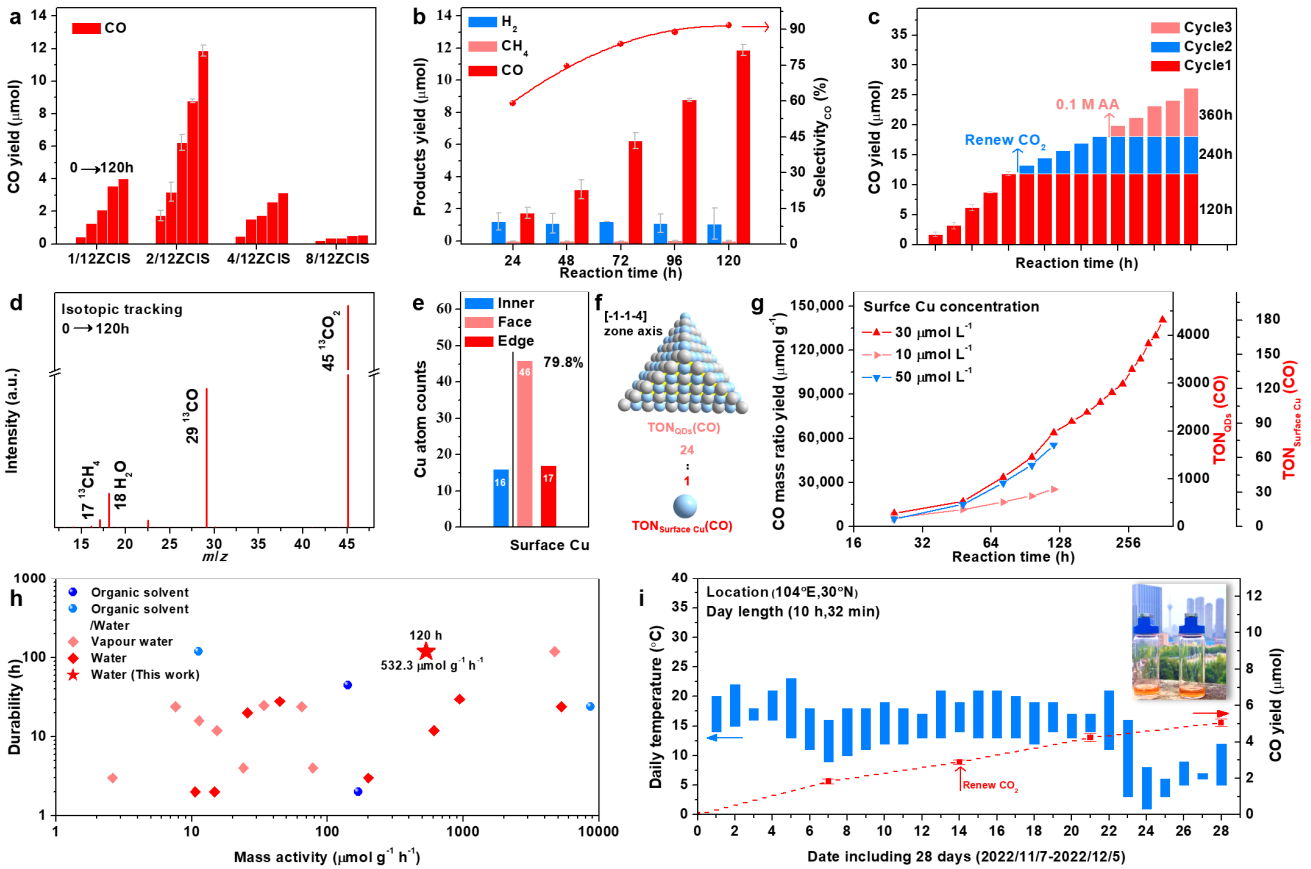

Figure 5. The CO_2-CO photoreduction performance. (a) CO yield of the prepared QDs recorded every 24 h during 120 h solar simulator illumination (380<λ<780 nm, 100 mW cm^{-2}). (b) CO, CH_4 and H_2 evolution yield and the selectivity of CO for 2/12ZCIS QDs. (c) Cycle test of CO yield for 2/12ZCIS QDs. (d) GC-MS spectrum of gas-phase products of $^{13}CO_2$ photoreduction for 2/12ZCIS QDs. (e) Statistics of surface copper catalytic sites and (f) TON correlation between numbers of QDs and surface copper atoms. (g) CO yield rates, TON_{QDs} (CO) and $TON_{surface\ Cu}$ (CO) of 2/12ZCIS QDs containing variable surface Cu concentration. (h) Efficiency and durability benchmarks of the previously reported photocatalysts for CO_2 photoreduction to CO. The statistical performance parameters are shown in Table S10. (i) Natural sunlight-driven CO_2 reduction performance of 2/12ZCIS QDs in 28 days. Error bars are calculated from two runs; uncertainty is ≤5%.

The photocatalytic CO_2 conversion performance of as-prepared QDs was examined without any cocatalysts or additional photosensitizers and performed under solar simulator irradiation (380<λ<780 nm, 100 mW cm^{-2}) in 5 mL of CO_2-saturated pure water with ascorbic acid as sacrificial reagent. As shown in Figure 5a, the Type-C Cu-deficient 2/12ZCIS QD sample exhibits a remarkable CO yield up to 12.2 μmol after light illumination of 120 h, which is nearly 24-fold and 4-fold higher than those of Type-A stoichiometric 8/12ZCIS QDs (0.5 μmol) and Type-B Cu-deficient 4/12ZCIS QDs (3.1 μmol), respectively. The band structure of the synthesized QDs was estimated by using UV photoelectron spectroscopy (UPS, Figure S10-11), whereas both the VB/CB edges for all QDs are quite similar. The favorable conduction band minimum (CBM) for the 1/12ZCIS, 2/12ZCIS, 4/12ZCIS and 8/12ZCIS QDs is -0.85, -0.68, -0.83 and -0.90 V vs. RHE, respectively, thus the photogenerated electrons in CBM can be transferred to CO_2 for reduction reactions (Figure S12). These similar band structures of QDs imply that the observed diverse photocatalytic CO_2 conversion performance is principally derived from different intrinsic copper-related defect states rather than band position variation.

In the case of 2/12ZCIS QDs, the production of CO increases rapidly and is nearly linear with the irradiation time (Figure 5b), suggesting considerable photocatalytic durability up to 120 h. Except for H_2 and trace CH_4, no other byproducts were detected during CO_2 photoreduction and a high CO selectivity of 92% was eventually achieved. Moreover, the 2/12ZCIS sample can maintain about 70% initial activity in a long-term test even up to 360 h after renewing the reaction atmosphere and adding sacrificial agent again (Figure 5c). To verify the carbon source of the produced CO, the isotopic tracking was conducted using $^{13}CO_2$ (Figure 5d) and a characteristic fingerprint of m/z = 29 (^{13}CO) is clearly detected as the product by gas chromatography-mass spectrometry (GC-MS). Besides, negligible products were generated in the absence of either QDs or light irradiation, implying the main contribution of CO from CO_2 photoreduction (Table S9). To prove that electrons were supplied by the AA during catalytic reaction cycle, additional PL quenching experiments were conducted on the 2/12ZCIS QD sample. As shown in Figure S13a, the intensity of PL emission was gradually quenched after introduction of AA into the system. The kinetic

emission decay of the QDs became faster as well, which is consistent with the decreasing emission intensity (Figure S13b). Fitting results show that the average lifetime of 2/12ZCIS QDs dropped from 71.1 ns to 30.9 ns with AA concentrations of 400 mM (Table S8), corresponding to a calculated hole transfer rate (2.6×10^4 $s^{-1}mM^{-1}$) from QDs to AA (Figure S13c).

To evaluate the turnover number (TON) per single QD or surface copper atom, we calculated the proportion of surface copper atoms in a typical QD model proposed in Figure 2g and Figure S3. As exhibited in Figure 5e and Figure 5f, around 80% of copper exists in the form of surface states and a single QD contains about 24 surface copper atoms. After further optimization of surface-Cu concentration (i.e., optimizing the QD catalysts concentration), the 2/12ZCIS QDs ultimately produce CO with a TON_{QDs} of 4319 and a $TON_{surface\ Cu}$ of 178, respectively, and a prominent mass ratio yield of 140,544 μmol g^{-1} can be achieved after the longest irradiation of 360 h (Figure 5g).

In comparison to the recent reported state-of-the-art CO_2 photoreduction systems (Figure 5h), we found that both mass activity (~500 μmol g^{-1} h^{-1}) and durability (120 h) of our QD samples were competitive even without any organic solvent.[51-54] Meanwhile, as shown in Figure S14, the AQYs of 2/12ZCIS QDs were respectively determined to be 0.32% (400 nm), 0.25% (450 nm), 0.11% (500 nm) and 0.05% (550 nm), which were competitive to that of other reported heterogeneous photocatalysts (Table S10). The lower AQY in the longer irradiated wavelengths is ascribed to the decreased ability of visible absorption for longer wavelengths. Inspired by the superior performance,we further conducted outdoor CO_2 photoreduction experiments under natural sunlight and ambient temperature, as shown in Figure 5i. Remarkably, continuous and stable CO generation was realized in 28 days with a wide temperature range (2~23 ℃), suggesting that natural sunlight can be efficiently utilized for carbon neutralization by using our QDs system, paving the way for future potential industrial manufacturing.

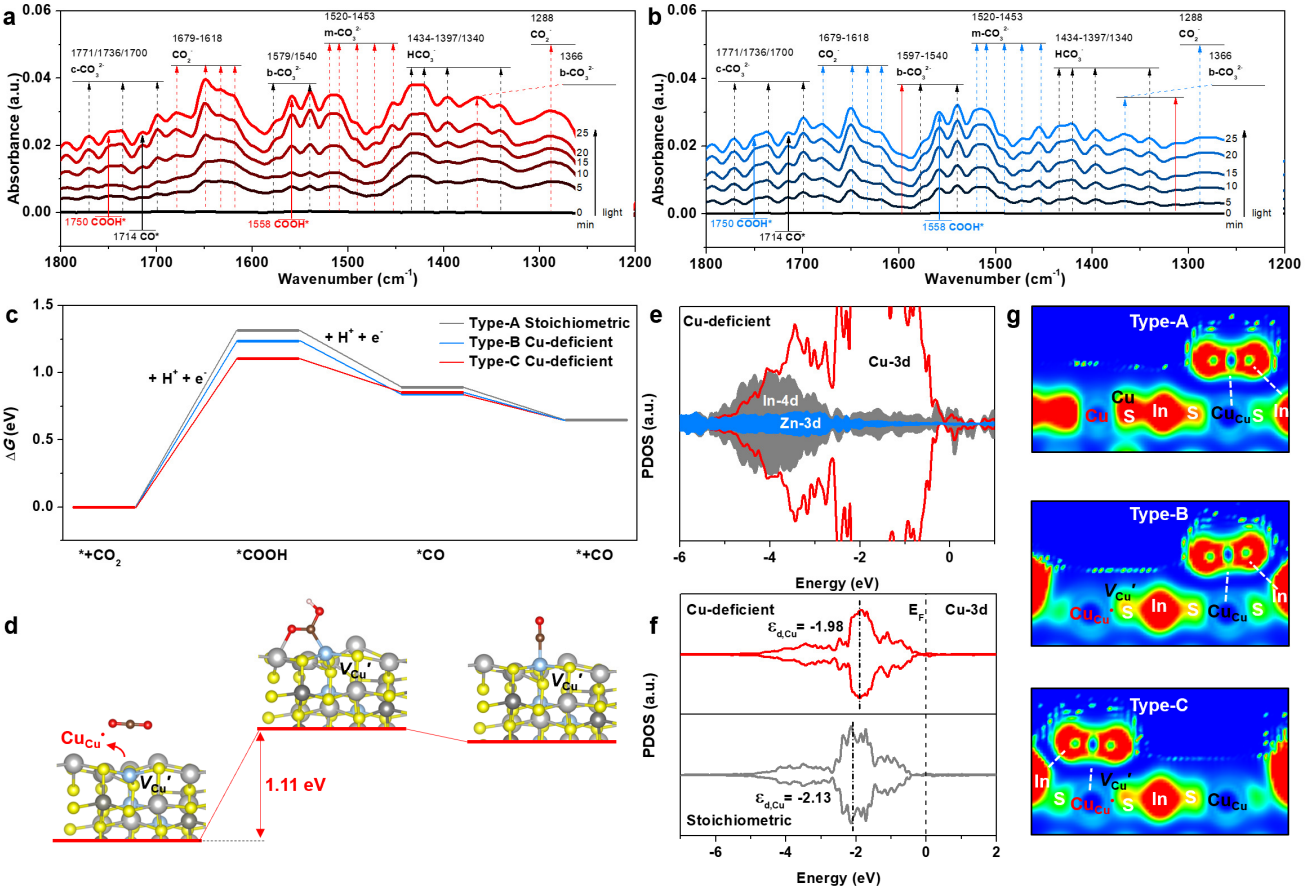

Figure 6. *In situ* DRIFTS and DFT calculations for photocatalytic CO_2-to-CO conversion. *In situ* DRIFTS of CO_2 and H_2O interaction with (a) 2/12ZCIS and (b) 4/12ZCIS QDs under constant simulated solar illumination. (c) Calculated free energy of the main reactions in photocatalytic CO_2 reduction using Type-A, B and C ZCIS QDs. (d) Key reaction configurations of CO_2 photoreduction to CO for Type-C Cu-deficient 2/12ZCIS QDs. The PDOS of (e) Cu-deficient ZCIS QDs. (f) The PDOS of Cu-3d for Cu-deficient and stoichiometric ZCIS QDs. (g) Electronic location function results of CO_2 molecule on the surface of Type-A (top), Type-B (middle) and Type-C (bottom) QD samples.

To elucidate the underlying mechanism for the superior performance of 2/12ZCIS QDs from CO_2 photoreduction to CO, the surface CO_2 adsorption, activation, and conversion processes were investigated by using *in situ* DRIFTS characterizations.

Figure 6a shows that the reaction intermediates on 2/12ZCIS QD samples are dynamically detected during 25 min light irradiation. Notably, the wide absorption bands (1800~1200 cm^{-1}) reflected the CO_2-derived species.[55] As shown in Figure 6a and Table S7, the monodentate carbonate (m-CO_3^{2-}, symmetric CO_3 stretching vibration ($\nu_s(CO_3)$): 1520~1453 cm^{-1}),[28, 55-60] bidentate (b-CO_3^{2-}, asymmetric CO_3 stretching vibration ($\nu_{as}(CO_3)$): 1579 and 1540 cm^{-1},[28, 46, 55-56, 59-61] $\nu_s(CO_3)$): 1366 cm^{-1})[55, 61] and chelating-bridged carbonate (c-CO_3^{2-}, ν(C-O): 1771, 1736 and 1700 cm^{-1})[28, 46, 55-56, 58] are apparent and strengthened with a prolonged illumination time. Further observation of bicarbonate HCO_3^- (σ(CHO): 1434~1397 and 1340 cm^{-1})[28, 55, 60-62] and carboxylate CO_2^- species (ν_s(O-C-O): 1679~1618 and 1288 cm^{-1})[45, 56, 63] confirm the surface-bound interaction between 2/12ZCIS QDs and the adsorbed CO_2. Most importantly, the peaks of COOH* (1750 and 1558 cm^{-1})[28, 57, 60, 64] and CO* (1714 cm^{-1})[28] intermediates (deemed as the crucial species for production of CO) became sharp with enhanced intensity, whereas the peaks of CH_2* (2923 cm^{-1})[28] and CH_3O* (2851 cm^{-1})[28] were negative and suggest the consumption of intermediates for hydrocarbons, which is consistent with the observed results of the trace CH_4 product (Figure S15). Additional peaks assigned to b-CO_3^{2-} appear and the intensity of b-CO_3^{2-} rather than CO_2^- peak accounts for the largest proportion in 4/12ZCIS QDs (Figure 6b).[55, 61] This is the essential fact that unavoidable accumulation of b-CO_3^{2-} species occurs due to the weak conversion of CO_2 to CO_2^- on the surface of 4/12ZCIS QDs. Carboxylate CO_2^- species were usually regarded to be activated easier for CO_2 reactant.[63, 65] These results suggest that the unique $Cu_{Cu}^{\bullet}$-V_{Cu}' defect pairs involved in 2/12ZCIS QDs have a tremendous influence on CO_2 conversion. On the basis of the *in-situ* DRIFTS results, we propose the CO_2 photoreduction pathways as follows:

$$CO_2 + * \rightarrow CO_2^* \quad (5)$$

$$CO_2^* + e^- + H^+ \rightarrow COOH^* \quad (6)$$

$$COOH^* + e^- + H^+ \rightarrow CO^* + H_2O \quad (7)$$

$$CO^* \rightarrow CO\uparrow + * \quad (8)$$

where the asterisks denote active sites, such as Cu-related defect states in this work, and the vertical arrows represent the release of the gas product.

To further support this conclusion, we conducted DFT calculation studies for CO_2 conversion in our QD systems. According to the calculated Gibbs free energy (ΔG) in Figure 6c, it is revealed that the formation of COOH* intermediates is the rate-limiting step for all samples, due to the endergonic process with high energy input.[62, 66-67] The initial hydrogenation pathway from CO_2 to COOH* requires overcoming a crucial activation energy barrier, whereas the Type-C Cu-deficient QDs have a lower COOH* formation energy of 1.11 eV than other QD samples, which might be ascribed to the abundant adjacent $Cu_{Cu}^{\bullet}$-V_{Cu}' defect pairs. As shown in Figure 6d and Figure S16, the introduction of V_{Cu}' defects can result in charge enrichment on the nearby surface Cu and In atoms of QDs such as the $Cu_{Cu}^{\bullet}$ sites,[14, 68] which serve as photoexcited electron transfer centers for the activation of CO_2. Meanwhile, the V_{Cu}' sites capture the VB hole to suppress the charge recombination, promoting the formation of COOH* species. Afterwards, the $Cu_{Cu}^{\bullet}$ and nearby In atoms can stabilize the rate-limiting COOH* intermediates with the Cu-In dual sites for effective CO_2 photoreduction[62]. We further investigated the partial density of states (PDOS) reflecting *d*-band center (ε_d), which demonstrated that the *d*-band has main contribution from Cu-3d, as shown in Figure 6e.[69-70] Specifically, the $\varepsilon_{d,Cu}$ (-1.98 eV) of Cu-deficient samples move further towards the Fermi level (E_F) than that of the stoichiometric samples ($\varepsilon_{d,Cu}$ =-2.13 eV) and the $\varepsilon_{d,In}$ upshifts from -4.16 eV to -3.91 eV (Figure 6f and Figure S17). According to the theory of Nørskov, the adsorbate-metal interaction becomes stronger when the ε_d shifts closer towards the E_F,[38, 69, 71] implying that the Cu and In sites close to V_{Cu}' sites enables the enhanced adsorption ability. The electronic location function results (Figure 6g) further verified this hypothesis, wherein the stoichiometric reaction domain (Type A, top) exhibits less variation in band angle and CO_2 molecule bending than other two reaction domains of Cu-deficient samples.[28, 55] In comparison, we can observe vital interactions between the $Cu_{Cu}^{\bullet}$-V_{Cu}' defect pairs and the adsorbed CO_2 molecule in Cu-deficient reaction domain (Type C, bottom), confirming the superiority of the $Cu_{Cu}^{\bullet}$-V_{Cu}' defect sites as an efficient CO_2 adsorption and activation model. Combining the previous calculation in Figure 1d, a larger number of electron transfer is recorded with the Type-C Cu-deficient reaction domain (0.015 e^- per CO_2 molecular). Hence, our DFT calculations manifest the reaction mechanism and clarify the defect-defect interaction of ZCIS QDs photocatalysts for efficient CO_2 photoreduction to CO.

3. CONCLUSION

In summary, a model of highly reactive domains in Cu-deficient colloidal ZCIS QDs was rationally constructed by precisely manipulating the intrinsic Cu-related defect states. Through tailoring the non-stoichiometric Cu content, the reactive domains of the Cu^{2+} defect states accompanied by copper vacancy (i.e., $Cu_{Cu}^{\bullet}$-V_{Cu}' defect pairs) are constructed in the ZCIS QDs for high-efficiency CO_2 photoreduction. The fs-TA and tr-PL spectra demonstrated that such $Cu_{Cu}^{\bullet}$-V_{Cu}' defect pairs in ZCIS QDs can optimize the photogenerated charge carrier kinetics, thus favoring the long-lived active charge separation/transfer and suppressing the nonradiative SRH recombination. The combination of *in situ* DRIFTS experiments and DFT calculations enables the understanding of dynamic intermediate-determining CO_2 photoreduction processes at molecular level. As a result, the Cu-deficient 2/12ZCIS QDs with abundant $Cu_{Cu}^{\bullet}$-V_{Cu}' defect pairs exhibited a high photocatalytic activity for CO_2 reduction to CO with a rate of 400~500 μmol g^{-1} h^{-1}. This work demonstrates that manipulating the intrinsic Cu-related defect states can tune both the photo-physical properties and catalytic-chemical processes for highly efficient CO_2 photoreduction, paving the way for precise defect states engineering for high-efficiency solar-to-fuel energy conversion.

AUTHOR INFORMATION

Corresponding Authors

Xin Tong - Institute of Fundamental and Frontier Sciences, University of Electronic Science and Technology of China,, Chengdu 610054, China; Yangtze Delta Region Institute (Huzhou), University of Electronic Science and Technology of China, Huzhou 313001, China

E-mail: xin.tong@uestc.edu.cn

Zhiming M. Wang - Institute of Fundamental and Frontier Sciences, University of Electronic Science and Technology of China, Chengdu 610054, China; Yangtze Delta Region Institute (Huzhou), University of Electronic Science and Technology of China, Huzhou 313001, China; Institute for Advanced Study, Chengdu University, Chengdu 610106, China

E-mail: zhmwang@uestc.edu.cn

Authors

Mengke Cai - Institute of Fundamental and Frontier Sciences, University of Electronic Science and Technology of China, Chengdu 610054, China; Yangtze Delta Region Institute (Huzhou), University of Electronic Science and Technology of China, Huzhou 313001, China

Peisen Liao - MOE Laboratory of Bioinorganic and Synthetic Chemistry, Lehn Institute of Functional Materials, School of Chemistry, Sun Yat-Sen University, Guangzhou 510275, China

Shujie Shen - Institute of Fundamental and Frontier Sciences, University of Electronic Science and Technology of China, Chengdu 610054, China

Hongyang Zhao - Institute of Fundamental and Frontier Sciences, University of Electronic Science and Technology of China, Chengdu 610054, China

Xin Li - Institute of Fundamental and Frontier Sciences, University of Electronic Science and Technology of China, Chengdu 610054, China

Li Xia - Institute of Fundamental and Frontier Sciences, University of Electronic Science and Technology of China, Chengdu 610054, China

Huaqian Zhi - Institute of Fundamental and Frontier Sciences, University of Electronic Science and Technology of China, Chengdu 610054, China

Nan Zhou - Institute of Fundamental and Frontier Sciences, University of Electronic Science and Technology of China, Chengdu 610054, China

Ziqian Xue - Institute for Integrated Cell-Material Sciences, Kyoto University, Kyoto 606-8501, Japan

Lei Jin - Institute of Fundamental and Frontier Sciences, University of Electronic Science and Technology of China, Chengdu 610054, China; Centre for Energy, Materials and Telecommunications, Institut national de la Recherche Scientifique, Varennes J3X 1P7, Canada

Jieyuan Li - Institute of Fundamental and Frontier Sciences, University of Electronic Science and Technology of China, Chengdu 610054, China

Guangqin Li - MOE Laboratory of Bioinorganic and Synthetic Chemistry, Lehn Institute of Functional Materials, School of Chemistry, Sun Yat-Sen University, Guangzhou 510275, China

Fan Dong - Institute of Fundamental and Frontier Sciences, University of Electronic Science and Technology of China, Chengdu 610054, China

Andrei V. Kabashin - Aix-Marseille University, Centre national de la recherche scientifique, Marseille 13009, France

Author Contributions

The manuscript was written through contributions of all authors. M.C. conceived the idea, organised the collaboration, conducted experiments, analysed the data, and wrote the draft manuscript. P. L., S. S., H.Z., X.L., L. X., H. Z. and N. Z. assisted in device optimisation and data analysis. Z. X., J. L., G. L., F. D., and X. T. helped to the idea and manuscript preparation. Z. M. W. and X. T. designed and supervised the project, directed the research, and contributed to the writing of the manuscript.

Notes

The authors declare no competing financial interest.

ASSOCIATED CONTENT

Supporting Information.

The Supporting Information is available free of charge at http://pubs.acs.org.
Materials and instrumentation, synthetic procedures, photocatalysis procedures, TEM images, PXRD, fs-TA, *In situ* DRIFTS, DFT Calculation, ICP-OES, UV-vis and PL spectra, XPS, UPS.

ACKNOWLEDGMENT

X.T. acknowledges the support from National Key Research and Development Program of China (No. 2019YFE0121600), National Natural Science Foundation of China (No. 22105031, 62011530131) and Sichuan Science and Technology Program (No. 2021YFH0054, 2023JDGD0011). Z.M.W. is grateful to the National Key Research and Development Program of China (No. 2019YFB2203400) and the "111 Project" (No. B20030). L. J. acknowledges the Young Scientists Fund of the National Natural Science Foundation of China (No. 22005044). The first author would like to thank his wife Jiayuan Yang for her companion and dedication. The authors would like to thank Zhang San from Shiyanjia Lab (www.shiyanjia.com) for the DFT analysis. The authors would like to thank the Materials Characterization Center of ECNU Multifunctional Platform for Innovation for the fs-TA tests.

REFERENCES

(1) Li, X.-B.; Tung, C.-H.; Wu, L.-Z. Semiconducting quantum dots for artificial photosynthesis. *Nat. Rev. Chem.* **2018,** *2*, 160-173.
(2) Wang, Q.; Pornrungroj, C.; Linley, S.; Reisner, E. Strategies to improve light utilization in solar fuel synthesis. *Nat. Energy* **2021,** *7*, 13-24.
(3) Li, X.; Tong, X.; Yue, S.; Liu, C.; Channa, A. I.; You, Y.; Wang, R.; Long, Z.; Zhang, Z.; Zhao, Z.; Liu, X.-F.; Wang, Z. M. Rational design of colloidal $AgGaS_2$/CdSeS core/shell quantum dots for solar energy conversion and light detection. *Nano Energy* **2021,** *89*, 106392.
(4) Wagner, A.; Sahm, C. D.; Reisner, E. Towards molecular understanding of local chemical environment effects in electro- and photocatalytic CO_2 reduction. *Nat. Catal.* **2020,** *3*, 775-786.
(5) Lan, G.; Fan, Y.; Shi, W.; You, E.; Veroneau, S. S.; Lin, W. Biomimetic active sites on monolayered metal–organic frameworks for artificial photosynthesis. *Nat. Catal.* **2022,** *5*, 1006-1018.
(6) Kong, T.; Jiang, Y.; Xiong, Y. Photocatalytic CO_2 conversion: What can we learn from conventional CO_x hydrogenation? *Chem. Soc. Rev.* **2020,** *49*, 6579-6591.
(7) Kim, J. H.; Hansora, D.; Sharma, P.; Jang, J. W.; Lee, J. S. Toward practical solar hydrogen production - an artificial photosynthetic leaf-to-farm challenge. *Chem. Soc. Rev.* **2019,** *48*, 1908-1971.
(8) Chen, X.; Liu, L.; Huang, F. Black titanium dioxide (TiO_2) nanomaterials. *Chem. Soc. Rev.* **2015,** *44*, 1861-1885.
(9) Park, J. S.; Kim, S.; Xie, Z.; Walsh, A. Point defect engineering in thin-film solar cells. *Nat. Rev. Mater.* **2018,** *3*, 194-210.
(10) Chen, R.; Ren, Z.; Liang, Y.; Zhang, G.; Dittrich, T.; Liu, R.; Liu, Y.; Zhao, Y.; Pang, S.; An, H.; Ni, C.; Zhou, P.; Han, K.; Fan, F.; Li, C. Spatiotemporal imaging of charge transfer in photocatalyst particles. *Nature* **2022,** *610*, 296-301.
(11) Chen, R.; Pang, S.; An, H.; Dittrich, T.; Fan, F.; Li, C. Giant Defect-Induced Effects on Nanoscale Charge Separation in Semiconductor Photocatalysts. *Nano Lett.* **2019,** *19*, 426-432.
(12) Wang, Y.; Han, P.; Lv, X.; Zhang, L.; Zheng, G. Defect and Interface Engineering for Aqueous Electrocatalytic CO_2 Reduction. *Joule* **2018,** *2*, 2551-2582.
(13) Zhu, W.; Zhang, L.; Yang, P.; Hu, C.; Dong, H.; Zhao, Z.-J.; Mu, R.; Gong, J. Formation of Enriched Vacancies for Enhanced CO_2 Electrocatalytic Reduction over AuCu Alloys. *ACS Energy Lett.* **2018,** *3*, 2144-2149.
(14) Li, S.; Duan, H.; Yu, J.; Qiu, C.; Yu, R.; Chen, Y.; Fang, Y.; Cai, X.; Yang, S. Cu Vacancy Induced Product Switching from Formate to CO for CO_2 Reduction on Copper Sulfide. *ACS Catal.* **2022,** *12*, 9074-9082.
(15) Wang, Z.; Zhang, L.; Schulli, T. U.; Bai, Y.; Monny, S. A.; Du, A.; Wang, L. Identifying Copper Vacancies and Their Role in the CuO Based Photocathode for Water Splitting. *Angew. Chem., Int. Ed.* **2019,** *58*, 17604-17609.
(16) Guo, N.; Xue, H.; Bao, A.; Wang, Z.; Sun, J.; Song, T.; Ge, X.; Zhang, W.; Huang, K.; He, F.; Wang, Q. Achieving Superior Electrocatalytic Performance by Surface Copper Vacancy Defects during Electrochemical Etching Process. *Angew. Chem., Int. Ed.* **2020,** *59*, 13778-13784.
(17) Kröger, F. A.; Vink, H. J. Relations between the Concentrations of Imperfections in Crystalline Solids. *Solid State Physics* **1956,** *3*, 307-435.
(18) Wang, J.; Bo, T.; Shao, B.; Zhang, Y.; Jia, L.; Tan, X.; Zhou, W.; Yu, T. Effect of S vacancy in Cu_3SnS_4 on high selectivity and activity of photocatalytic CO_2 reduction. *Appl. Catal., B* **2021,** *297*, 120498.
(19) Tsuji, M.; Iimura, S.; Kim, J.; Hosono, H. Hole Concentration Reduction in CuI by Zn Substitution and its Mechanism: Toward Device Applications. *ACS Appl. Mater. Interfaces* **2022,** *14*, 33463-33471.
(20) Sequeda, I. N.; Melendez, A. M. Understanding the Role of Copper Vacancies in Photoelectrochemical CO_2 Reduction on Cuprous Oxide. *J. Phys. Chem. Lett.* **2022,** *13*, 3667-3673.
(21) Xia, L.; Tong, X.; Li, X.; Imran Channa, A.; You, Y.; Long, Z.; Vomiero, A.; Wang, Z. M. Synergistic tailoring of band structure and charge carrier extraction in "green" core/shell quantum dots for highly efficient solar energy conversion. *Chem. Eng. J.* **2022,** *442*, 136214.
(22) Zhou, N.; Zhao, H.; Li, X.; Li, P.; You, Y.; Cai, M.; Xia, L.; Zhi, H.; Channa, A. I.; Wang, Z. M.; Tong, X. Activating Earth-Abundant Element-Based Colloidal Copper Chalcogenide Quantum Dots for Photodetector and Optoelectronic Synapse Applications. *ACS Mater. Lett.* **2023,** *5*, 1209-1218.
(23) Brovelli, S.; Galland, C.; Viswanatha, R.; Klimov, V. I. Tuning radiative recombination in Cu-doped nanocrystals via electrochemical control of surface trapping. *Nano Lett.* **2012,** *12*, 4372-4379.
(24) Jara, D. H.; Stamplecoskie, K. G.; Kamat, P. V. Two Distinct Transitions in Cu_xInS_2 Quantum Dots. Bandgap versus Sub-Bandgap Excitations in Copper-Deficient Structures. *J. Phys. Chem. Lett.* **2016,** *7*, 1452-1459.

(25) Fuhr, A. S.; Yun, H. J.; Makarov, N. S.; Li, H.; McDaniel, H.; Klimov, V. I. Light Emission Mechanisms in $CuInS_2$ Quantum Dots Evaluated by Spectral Electrochemistry. *ACS Photonics* **2017,** *4*, 2425-2435.
(26) van der Stam, W.; de Graaf, M.; Gudjonsdottir, S.; Geuchies, J. J.; Dijkema, J. J.; Kirkwood, N.; Evers, W. H.; Longo, A.; Houtepen, A. J. Tuning and Probing the Distribution of Cu^+ and Cu^{2+} Trap States Responsible for Broad-Band Photoluminescence in $CuInS_2$ Nanocrystals. *ACS Nano* **2018,** *12*, 11244-11253.
(27) Fuhr, A.; Yun, H. J.; Crooker, S. A.; Klimov, V. I. Spectroscopic and Magneto-Optical Signatures of Cu^{1+} and Cu^{2+} Defects in Copper Indium Sulfide Quantum Dots. *ACS Nano* **2020,** *14*, 2212-2223.
(28) Sheng, J.; He, Y.; Huang, M.; Yuan, C.; Wang, S.; Dong, F. Frustrated Lewis Pair Sites Boosting CO_2 Photoreduction on Cs_2CuBr_4 Perovskite Quantum Dots. *ACS Catal.* **2022,** *12*, 2915-2926.
(29) Cai, M.; Li, X.; Zhao, H.; Liu, C.; You, Y.; Lin, F.; Tong, X.; Wang, Z. M. Decoration of $BiVO_4$ Photoanodes with Near-Infrared Quantum Dots for Boosted Photoelectrochemical Water Oxidation. *ACS Appl. Mater. Interfaces* **2021,** *13*, 50046-50056.
(30) Cai, M.; Tong, X.; Zhao, H.; Li, X.; You, Y.; Wang, R.; Xia, L.; Zhou, N.; Wang, L.; Wang, Z. M. Ligand-Engineered Quantum Dots Decorated Heterojunction Photoelectrodes for Self-Biased Solar Water Splitting. *Small* **2022,** *18*, 2204495.
(31) He, Y.; Zhang, L.; Xiong, H.-W.; Kang, X. Evolution of lattice defects in nickel ferrite spinel: Oxygen vacancy and cation substitution. *J. Alloys Compd.* **2022,** *917*, 165494.
(32) Wang, R.; Tong, X.; Long, Z.; Channa, A. I.; Zhao, H.; Li, X.; Cai, M.; You, Y.; Sun, X.; Wang, Z. Rational design of eco-friendly Mn-doped nonstoichiometric CuInSe/ZnSe core/shell quantum dots for boosted photoelectrochemical efficiency. *Nano Res.* **2022,** *15*, 7614–7621.
(33) Cai, M.; Liu, Q.; Xue, Z.; Li, Y.; Fan, Y.; Huang, A.; Li, M.-R.; Croft, M.; Tyson, T. A.; Ke, Z.; Li, G. Constructing 2D MOFs from 2D LDHs: a highly efficient and durable electrocatalyst for water oxidation. *J. Mater. Chem. A* **2020,** *8*, 190-195.
(34) Cai, M.; Zhang, Y.; Zhao, Y.; Liu, Q.; Li, Y.; Li, G. Two-dimensional metal–organic framework nanosheets for highly efficient electrocatalytic biomass 5-(hydroxymethyl)furfural (HMF) valorization. *J. Mater. Chem. A* **2020,** *8*, 20386-20392.
(35) Peng, C.; Luo, G.; Zhang, J.; Chen, M.; Wang, Z.; Sham, T. K.; Zhang, L.; Li, Y.; Zheng, G. Double sulfur vacancies by lithium tuning enhance CO_2 electroreduction to n-propanol. *Nat. Commun.* **2021,** *12*, 1580.
(36) Liu, G.; Zheng, F.; Li, J.; Zeng, G.; Ye, Y.; Larson, D. M.; Yano, J.; Crumlin, E. J.; Ager, J. W.; Wang, L.-w.; Toma, F. M. Investigation and mitigation of degradation mechanisms in Cu_2O photoelectrodes for CO_2 reduction to ethylene. *Nat. Energy* **2021,** *6*, 1124-1132.
(37) Weng, Z.; Wu, Y.; Wang, M.; Jiang, J.; Yang, K.; Huo, S.; Wang, X. F.; Ma, Q.; Brudvig, G. W.; Batista, V. S.; Liang, Y.; Feng, Z.; Wang, H. Active sites of copper-complex catalytic materials for electrochemical carbon dioxide reduction. *Nat. Commun.* **2018,** *9*, 415.
(38) Xue, Z.; Liu, K.; Liu, Q.; Li, Y.; Li, M.; Su, C. Y.; Ogiwara, N.; Kobayashi, H.; Kitagawa, H.; Liu, M.; Li, G. Missing-linker metal-organic frameworks for oxygen evolution reaction. *Nat. Commun.* **2019,** *10*, 5048.
(39) Pastor, E.; Sachs, M.; Selim, S.; Durrant, J. R.; Bakulin, A. A.; Walsh, A. Electronic defects in metal oxide photocatalysts. *Nat. Rev. Mater.* **2022,** *7*, 503-521.
(40) Du, J.; Singh, R.; Fedin, I.; Fuhr, A. S.; Klimov, V. I. Spectroscopic insights into high defect tolerance of Zn:$CuInSe_2$ quantum-dot-sensitized solar cells. *Nat. Energy* **2020,** *5*, 409-417.
(41) Jeong, S.; Ko, M.; Jeong, S.; Shin, S. Y.; Park, S. M.; Do, Y. R.; Song, J. K. Optical Transitions of $CuInS_2$ Nanoparticles: Two Types of Absorption and Two Types of Emission. *J. Phys. Chem. C* **2020,** *124*, 14400-14408.
(42) Berends, A. C.; Rabouw, F. T.; Spoor, F. C.; Bladt, E.; Grozema, F. C.; Houtepen, A. J.; Siebbeles, L. D.; de Mello Donega, C. Radiative and Nonradiative Recombination in $CuInS_2$ Nanocrystals and $CuInS_2$-Based Core/Shell Nanocrystals. *J. Phys. Chem. Lett.* **2016,** *7*, 3503-3509.
(43) Wolff, C. M.; Frischmann, P. D.; Schulze, M.; Bohn, B. J.; Wein, R.; Livadas, P.; Carlson, M. T.; Jäckel, F.; Feldmann, J.; Würthner, F.; Stolarczyk, J. K. All-in-one visible-light-driven water splitting by combining nanoparticulate and molecular co-catalysts on CdS nanorods. *Nat. Energy* **2018,** *3*, 862-869.
(44) Wu, K.; Zhu, H.; Liu, Z.; Rodriguez-Cordoba, W.; Lian, T. Ultrafast charge separation and long-lived charge separated state in photocatalytic CdS-Pt nanorod heterostructures. *J. Am. Chem. Soc.* **2012,** *134*, 10337-10340.
(45) Cheng, L.; Yue, X.; Fan, J.; Xiang, Q. Site-Specific Electron-Driving Observations of CO_2 -to-CH_4 Photoreduction on Co-doped CeO_2 /Crystalline Carbon Nitride S-scheme Heterojunctions. *Adv. Mater.* **2022,** *34*, 2200929.
(46) Cheng, L.; Yue, X.; Wang, L.; Zhang, D.; Zhang, P.; Fan, J.; Xiang, Q. Dual-Single-Atom Tailoring with Bifunctional Integration for High-Performance CO_2 Photoreduction. *Adv. Mater.* **2021,** *33*, 2105135.
(47) Wang, Q.; Domen, K. Particulate Photocatalysts for Light-Driven Water Splitting: Mechanisms, Challenges, and Design Strategies. *Chem. Rev.* **2020,** *120*, 919-985.
(48) Wang, W.; Bai, X.; Ci, Q.; Du, L.; Ren, X.; Phillips, D. L. Near‐Field Drives Long‐Lived Shallow Trapping of Polymeric C_3N_4 for Efficient Photocatalytic Hydrogen Evolution. *Adv. Funct. Mater.* **2021,** *31*, 2103978.
(49) Corp, K. L.; Schlenker, C. W. Ultrafast Spectroscopy Reveals Electron-Transfer Cascade That Improves Hydrogen Evolution with Carbon Nitride Photocatalysts. *J. Am. Chem. Soc.* **2017,** *139*, 7904-7912.
(50) Zhao, H.; Wang, W.; Li, X.; Li, P.; Cai, M.; You, Y.; Wang, R.; Channa, A. I.; Tong, X.; Wang, Z. M. Engineering the Interfacial Structure of Heavy Metal‐Free Colloidal Heterostructured Quantum Dots for High‐Efficiency Photoelectrochemical Water Oxidation without Co-Catalyst. *Adv. Energy Sustainability Res.* **2022,** *4*, 2200142.
(51) Huang, N. Y.; Shen, J. Q.; Zhang, X. W.; Liao, P. Q.; Zhang, J. P.; Chen, X. M. Coupling Ruthenium Bipyridyl and Cobalt Imidazolate Units in a Metal-Organic Framework for an Efficient Photosynthetic Overall Reaction in Diluted CO_2. *J. Am. Chem. Soc.* **2022,** *144*, 8676-8682.
(52) Yu, B.; Meng, T.; Ding, X.; Liu, X.; Wang, H.; Chen, B.; Zheng, T.; Li, W.; Zeng, Q.; Jiang, J. Hydrogen-Bonded Organic Framework Ultrathin Nanosheets for Efficient Visible-Light Photocatalytic CO_2 Reduction. *Angew. Chem., Int. Ed.* **2022,** *61*, e202211482.

(53) Yang, G.; Li, S.; Li, N.; Zhang, P.; Su, C.; Gong, L.; Chen, B.; Qu, C.; Qi, D.; Wang, T.; Jiang, J. Enhanced Photocatalytic CO_2 Reduction through Hydrophobic Microenvironment and Binuclear Cobalt Synergistic Effect in Metallogels. *Angew. Chem., Int. Ed.* **2022,** *61*, e202205585.
(54) Pugliese, E.; Gotico, P.; Wehrung, I.; Boitrel, B.; Quaranta, A.; Ha-Thi, M. H.; Pino, T.; Sircoglou, M.; Leibl, W.; Halime, Z.; Aukauloo, A. Dissection of Light-Induced Charge Accumulation at a Highly Active Iron Porphyrin: Insights in the Photocatalytic CO_2 Reduction. *Angew. Chem., Int. Ed.* **2022,** *61*, e202117530.
(55) Sheng, J.; He, Y.; Li, J.; Yuan, C.; Huang, H.; Wang, S.; Sun, Y.; Wang, Z.; Dong, F. Identification of Halogen-Associated Active Sites on Bismuth-Based Perovskite Quantum Dots for Efficient and Selective CO_2-to-CO Photoreduction. *ACS Nano* **2020,** *14*, 13103-13114.
(56) Shi, X.; Dong, X. a.; He, Y.; Yan, P.; Zhang, S.; Dong, F. Photoswitchable Chlorine Vacancies in Ultrathin $Bi_4O_5Cl_2$ for Selective CO_2 Photoreduction. *ACS Catal.* **2022,** *12*, 3965-3973.
(57) Chen, X.; Peng, C.; Dan, W.; Yu, L.; Wu, Y.; Fei, H. Bromo- and iodo-bridged building units in metal-organic frameworks for enhanced carrier transport and CO_2 photoreduction by water vapor. *Nat. Commun.* **2022,** *13*, 4592.
(58) Wang, R.; Wang, X.; Xiong, Y.; Hou, Y.; Wang, Y.; Ding, J.; Zhong, Q. Modulation of Trivalent/Tetravalent Metallic Elements in Ni-Based Layered Double Hydroxides for Photocatalytic CO_2 Reduction. *ACS Appl. Mater. Interfaces* **2022,** *14*, 35654-35662.
(59) Lei, B.; Cui, W.; Chen, P.; Chen, L.; Li, J.; Dong, F. C–Doping Induced Oxygen-Vacancy in WO_3 Nanosheets for CO_2 Activation and Photoreduction. *ACS Catal.* **2022,** *12*, 9670-9678.
(60) Zhou, J.; Li, J.; Kan, L.; Zhang, L.; Huang, Q.; Yan, Y.; Chen, Y.; Liu, J.; Li, S. L.; Lan, Y. Q. Linking oxidative and reductive clusters to prepare crystalline porous catalysts for photocatalytic CO_2 reduction with H_2O. *Nat. Commun.* **2022,** *13*, 4681.
(61) Yu, Y.; Dong, X.; Chen, P.; Geng, Q.; Wang, H.; Li, J.; Zhou, Y.; Dong, F. Synergistic Effect of Cu Single Atoms and Au-Cu Alloy Nanoparticles on TiO_2 for Efficient CO_2 Photoreduction. *ACS Nano* **2021,** *15*, 14453-14464.
(62) Li, X.; Sun, Y.; Xu, J.; Shao, Y.; Wu, J.; Xu, X.; Pan, Y.; Ju, H.; Zhu, J.; Xie, Y. Selective visible-light-driven photocatalytic CO_2 reduction to CH4 mediated by atomically thin $CuIn_5S_8$ layers. *Nat. Energy* **2019,** *4*, 690-699.
(63) Liu, L.; Jiang, Y.; Zhao, H.; Chen, J.; Cheng, J.; Yang, K.; Li, Y. Engineering Coexposed {001} and {101} Facets in Oxygen-Deficient TiO2 Nanocrystals for Enhanced CO_2 Photoreduction under Visible Light. *ACS Catal.* **2016,** *6*, 1097-1108.
(64) Lin, X.; Xia, S.; Zhang, L.; Zhang, Y.; Sun, S.; Chen, Y.; Chen, S.; Ding, B.; Yu, J.; Yan, J. Fabrication of Flexible Mesoporous Black Nb_2O_5 Nanofiber Films for Visible-Light-Driven Photocatalytic CO_2 Reduction into CH_4. *Adv. Mater.* **2022,** *34*, 2200756.
(65) Pu, Y.; Luo, Y.; Wei, X.; Sun, J.; Li, L.; Zou, W.; Dong, L. Synergistic effects of Cu_2O-decorated CeO_2 on photocatalytic CO_2 reduction: Surface Lewis acid/base and oxygen defect. *Appl. Catal., B* **2019,** *254*, 580-586.
(66) Wang, F.; Hou, T.; Zhao, X.; Yao, W.; Fang, R.; Shen, K.; Li, Y. Ordered Macroporous Carbonous Frameworks Implanted with CdS Quantum Dots for Efficient Photocatalytic CO_2 Reduction. *Adv. Mater.* **2021,** *33*, 2102690.
(67) Xin, Z. K.; Gao, Y. J.; Gao, Y.; Song, H. W.; Zhao, J.; Fan, F.; Xia, A. D.; Li, X. B.; Tung, C. H.; Wu, L. Z. Rational Design of Dot-on-Rod Nano-Heterostructure for Photocatalytic CO_2 Reduction: Pivotal Role of Hole Transfer and Utilization. *Adv. Mater.* **2022,** *34*, 2106662.
(68) Jiao, X.; Chen, Z.; Li, X.; Sun, Y.; Gao, S.; Yan, W.; Wang, C.; Zhang, Q.; Lin, Y.; Luo, Y.; Xie, Y. Defect-Mediated Electron-Hole Separation in One-Unit-Cell $ZnIn_2S_4$ Layers for Boosted Solar-Driven CO_2 Reduction. *J. Am. Chem. Soc.* **2017,** *139*, 7586-7594.
(69) Shi, H.; Wang, H.; Zhou, Y.; Li, J.; Zhai, P.; Li, X.; Gurzadyan, G. G.; Hou, J.; Yang, H.; Guo, X. Atomically Dispersed Indium-Copper Dual-Metal Active Sites Promoting C-C Coupling for CO_2 Photoreduction to Ethanol. *Angew. Chem., Int. Ed.* **2022,** *61*, e202208904.
(70) Wang, G.; Chen, Z.; Wang, T.; Wang, D.; Mao, J. P and Cu Dual Sites on Graphitic Carbon Nitride for Photocatalytic CO_2 Reduction to Hydrocarbon Fuels with High C_2H_6 Evolution. *Angew. Chem., Int. Ed.* **2022,** *61*, e202210789.
(71) Sun, Y.; Xue, Z.; Liu, Q.; Jia, Y.; Li, Y.; Liu, K.; Lin, Y.; Liu, M.; Li, G.; Su, C. Y. Modulating electronic structure of metal-organic frameworks by introducing atomically dispersed Ru for efficient hydrogen evolution. *Nat. Commun.* **2021,** *12*, 1369.

Insert Table of Contents artwork here

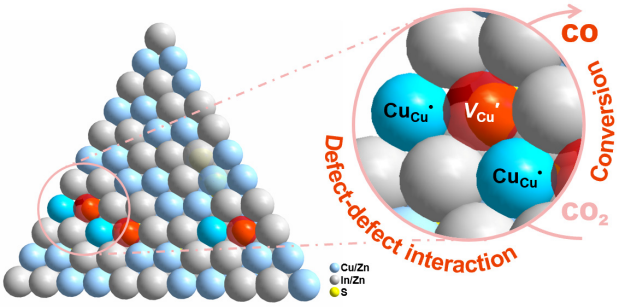

4.2 cm × 8.4 cm